Dalton Transactions

ROYAL SOCIETY OF CHEMISTRY

PAPER

View Article Online
View Journal | View Issue

Cite this: *Dalton Trans.*, 2022, **51**, 11515

Crystal phase modified blue upconversion on Tm^{3+}/Yb^{3+}:BCZT ceramic phosphor benefits multifunctionality in white-light applications†

Prasenjit Prasad Sukul * and Hendrik C. Swart *

Rare earth (RE) doped perovskite oxide hosts especially titanates, are promising phosphor materials in terms of white-light emission owing to their extraordinary properties such as an exceptional hosting environment for RE-ions and a switchable crystal phase near the phase boundary. Here, we report a new strategy of crystal phase modification to enhance the blue upconversion (UC) efficiency to such an extent that the combinational mixing of blue and green/red-emitting phosphor gives intense white emission. The Lead free $(Ba_{0.85}Ca_{0.15})(Zr,Ti)O_3$ ceramics were synthesised at different sintering temperatures by incorporation of Tm^{3+}/Yb^{3+} ions as dopants. The UC quantum efficiency of the Tm^{3+}/Yb^{3+}:BCZT sample sintered at 1300 °C was recorded at different excitation power densities. It was observed that the crystal phase transformation from tetragonal to rhombohedral symmetry in the sample near the phase boundary plays a cruicial role in improving the quantum efficiency. White-light emission applications were demonstrated by preparing biphasic samples with powder mixing of a BCZT:Tm^{3+}/Yb^{3+} (blue-emitting) + BCZT:Er^{3+}/Yb^{3+} (green/red-emitting) phosphor, and their composition were optimised at a mixed ratio. Thereafter, photometric characterization (CIE chromaticity, colour purity and corelated colour temperatures) was performed, and it indicated the suitability of the current biphasic samples in direct white-light (cooler) applications on an industrial scale. Crystal phase modified blue emission efficiency enhancement is a key feature of this work, which helps to generate approximately pure white-light with ideal chromacity (~0.333, 0.343) emission when Tm^{3+}/Yb^{3+}:BCZT is mixed with a green emitting BCZT:Er^{3+}/Yb^{3+} phosphor.

Received 21st June 2022,
Accepted 12th July 2022

DOI: 10.1039/d2dt01962k

rsc.li/dalton

1 Introduction

The research on upconversion (UC) fluorescent materials has come a long way in terms of their wide applicability areas,[1–7] and, in the last 61 years, significant contribution has been made by a wide community of researcher working day and night to explore more from the UC phenomena. Among the different applications of UC materials, a major research has been done on white LEDs[8–11] due to their potentiality to replace traditional light sources because of their following advantages, less hazardous to the environment, low energy consumption,[10] and longer lifespan.[11] Commonly, UC based white-light are generated in two basic methods (1) combining three independently optimized monochromatic phosphors (red, green and blue) in a proper mixing ratio in the presence of a mercury atmosphere, which was first introduced in 1996 by Downing *et al.*,[12] (2) direct synthesis of a single UC phosphor that converts infrared light into a mixture of RGB. The mercury, present inside the lamp, creates a UV light that excites the phosphor coating inside the walls of the bulb to emit visible light. The former method results into an unstable white-light due to difference in distinct degradation rates of each monochromatic phosphor. Noh *et al.* shown tridoped phosphors has biomedical and display device applications through upconversion in Y_2O_3 phosphors.[13] The march toward more environmentally friendly lighting involves the development of new phosphors and alternative processes. Recently, research interest has grown to fabricate single white-light phosphors by several lanthanide ion combinations. It has been exploited in sol–gel derived thin films[14] to avoid the intrinsic colour balance,[1] device complexity[15] and high cost associated with such multiple emitting components. The possible reason for the trend to switch into single white-light emitting phosphors can be realised through the fact, that although researcher have tried to modulate the Ln^{3+} ion concentration in different phosphor host materials and also tried various synthesis techniques, the obtained results are not satisfactory at this stage. As a majority of the synthesized phosphors has relevant limitations[16] since blue- and white-light emitters are not as efficient as the green and red ones. Therefore, if we can concentrate in improving the efficiency of blue-emitting phosphors, it may solve the problem.

Department of Physics, University of Free State, Bloemfontein 9300, Republic of South Africa. E-mail: sukul.pp@ufs.ac.za, swarthc@ufs.ac.za

† Electronic supplementary information (ESI) available. See DOI: https://doi.org/10.1039/d2dt01962k

The UC efficiency can be modified by changing the dopant or choosing an appropriate host material of low phonon energy, high transparency, and outstanding chemical and thermal stability. Host materials with low phonon energy may decrease the probability of nonradiative transitions, consequently leading to an increase in the UC efficiency. The UC luminescence (UCL) efficiency depends on the concentration and combination of dopants which define the number of luminescent centres as well as on their spatial distance in the host material lattice. It is reported that the UCL efficiency can be regulated by changing the crystal phase, size and morphology of the host matrix[17] and the possible solution lies here. Rare earth (RE) ions in a crystal experience electrostatic interaction and it is dependent on the position of the ion in the crystal and also the structure of the crystal. Same ions in various crystal structures of a compound give different emission intensity, such as Er^{3+} ions in β-NaYF4 give very high UC emission compared to the α-NaYF4. Tailoring the crystal field of lanthanide ions could be an effective strategy for enhancing the UCL of a wide variety of host materials. Despite recent progress in the development of UC material synthesis, the development of UC with enhanced efficiency is still inefficient, especially for blue-emitting materials. In our previous reports[18,19] it was observed that the crystal phase transformation in RE-ion doped perovskite phosphor not only changes its structural properties but also shows huge luminescence emission enhancement. Moreover, we have observed that the PL enhancements work as signature codes or spectroscopic probes to detect any crystal phase changes occurring in the sample, as predicted by Polman[20] in his findings exactly 21 years ago. Our investigations led us to the conclusion that RE-ion doped perovskite $Pb(Zr,Ti)O_3$(PZT) can be a good multifunctional host for observing crystal-phase-modified luminescence near the morphotropic phase boundary (MPB).[18] This material was extensively investigated because of its ultrahigh piezoelectric properties near the phase transition region (MPB), that is, the concurrence of rhombohedral- and tetragonal phases. PZT is the most widely used and investigated multifunctional material which possesses dielectric, piezoelectric, and electro-optic ceramics with diverse applications in industrial manufacturing, power production, transportation, consumer electronics, communication, medicine, and health care. However, in 2003, the European Union imposed a ban on the use of hazardous compounds in consumer items.[21] Because lead zirconate titanate ceramics contain 60% harmful PbO, it is recommended to substitute PbO with similar nontoxic materials because of these environment legislations.[22] Although serious work has been done on lead substitutes, very few of the reported Pb-free materials can compete with the PZT framework. As a consequence, a number of lead-free perovskite ceramics gathered considerable attention among researchers in recent years because of their eco-friendly behaviour.

BNT–BT ($Bi_{1/2}Na_{1/2}TiO_3$–$BaTiO_3$), KNN ($K_{1-x}Na_xNbO_3$), BCZT [$(Ba,Ca)(Zr,Ti)O_3$] and their co-doped counterparts are not only environment friendly but at the same time they also project good piezoelectric properties such as hard and soft PZT.[21,22] Among these alternatives, $BaTiO_3$ (BT)-based materials have been investigated because of their high piezoelectric constant d_{33} of pure BT which is ~190 pC N^{-1} with very high permittivity (~10^4–10^6). BT can be easily modified by the addition of appropriate dopants at different sites of the ABO_3 lattice or by varying the sintering temperatures.[23,24] Recently, large temperature tuning of RE ion-doped BT phosphors by PL and Raman studies was reported by De *et al.*[25] At room temperature, BCZT ceramics, which is a solid solution BT with $BaZrO_3$ or $CaTiO_3$, exhibits interesting phase transition behaviour and piezoelectric properties[26] *e.g.* a phase boundary between rhombohedral (BZT side) and tetragonal (BCT side) phases similar to solid state solutions of $PbZrO_3$ and $PbTiO_3$ to form PZT[18] at room temperature. Moreover, it also shows MPB boundary[27] and is also free from any volatile impurities such as the PZT framework discussed in our previous report.[18] In 2016, Wang *et al.*[28] reported strong luminescence and Piezo properties were observed from praseodymium (Pr) replacing BCZT ions at the A-site. Ramovatar *et al.*[29] also reported PL emission and structural property enhancement on Pr-doped BCZT. However, reports on UC luminescence on BCZT correlating with crystal phase studies have not yet reported. Exploring the crystal phase on multifunctional hosts such as BCZT will be of great interest, and there is a need to study optical tailoring properties to observe high UCL efficiency which is expected from BCZT. As our aim was to obtain white-light emission from a combinational phosphor material without the help of several RGB phosphors to avoid degrading loss, we have considered focusing on increasing the blue emission efficiency. Considering the probable high upconversion of the host and the broad range of colours achievable by proper RE dopant selection, attempts to produce white-light from this host are of significant technology interest.

The thulium (Tm^{3+}) activator ion gives a strong blue emission at approximately 489 nm, but it is observed only in hosts with a lower phonon frequency. However, like the Er^{3+} activator ion the Tm^{3+} ion has a smaller absorption cross-section. Therefore, for efficient blue upconversion, we need Yb^{3+} ions as sensitisers along with Tm^{3+} ions, as the ytterbium ion has a large absorption at 980 nm and can efficiently transfer its energy from $^2F_{5/2}$ level to the Tm^{3+} ion. There are very few reports where crystal-phase-tailored luminescence is observed in RE io-doped PZT, except for our previous reports.[18,19] Similarly, crystal phase modified luminescence emission has not been reported for Tm^{3+}/Yb^{3+} dopant combinations in BCZT hosts. These facts motivate us to study above combination for completing the objective of possible white-light generation using phase tailored blue upconversion.

In the present study, we report visible UC emission studies of Tm^{3+}/Yb^{3+} co-doped BCZT ceramic phosphors, where the substitution of BCZT-A site (Host) is replaced by Yb^{3+} and Tm^{3+} ions The replacement of the RE ions in the host follows the rule of substitution, such as charge compatibility and similarity of ionic radii. The blue UC emission efficiency, which was influenced by the crystal phase transformation occurring

in the sample, was tested. To generate white-light, the current blue-emitting phosphor is employed with a green/red-emitting phosphor of the same stoichiometry (BCZT:Er^{3+}/Yb^{3+}), which is optimised separately. Two powders, BCZT:Tm^{3+}/Yb^{3+} (blue emission) and BCZT:Er^{3+}/Yb^{3+} (green/red emission), were properly mixed using acetone-assisted grinding for 50 min in the second procedure. The biphasic samples generated by powder mixing are referred to as BCZT:Tm^{3+}/Yb^{3+} + BCZT:Er^{3+}/Yb^{3+} phosphor and their composition were optimised at a mixed ratio to generate white-light. Intense blue emission by using crystal phase modification was not studied in the past, especially for uniquely designed Tm^{3+}/Yb^{3+} co-doped BCZT ceramic phosphors. The Tm^{3+}/Yb^{3+}:BCZT ceramic phosphor was synthesized using a novel modified microwave-assisted solid-state reaction. Moreover, the photometric characterization (CIE, CCT, colour purity) of the current biphasic sample in terms of industrial lighting applications is carried out for its use as a commercial cooler white-light source.

2 Experimental

2.1 Materials and methods

Highly efficient blue emissive phosphor was synthesised by using a modified conventional solid-state reaction method through a microwave (MW) assisted solid state reaction with simultaneous multistage heating and drying. The detailed MW assisted multistage synthesis process is shown in the flowchart in Fig. 1. Reagent grade pure raw powders of $BaCO_3$, $CaCO_3$, TiO_2, ZrO_2 Tm_2O_3 and Yb_2O_3 from Sigma Aldrich (Germany) were used for the sample preparation. The RE ion concentrations of Tm^{3+} and Yb^{3+} were taken as 0.15 mol% and 2.0 mol%, respectively, to get the optimum luminescence output.[30] After being weighted in stoichiometric quantities, the starting materials were mixed with zirconia in isopropanol for 10 h in an agate mortar. The mixed slurry was then kept in a MW reactor oven (2.45 GHz frequency, 700 W power) for 5 h at 300 °C. This will create separate particles of the material that diffuse to the neighbouring powder particles, which is better than the calcination process. The advantage of MW heating over direct heat treatment is that the temperature profile of an MW material is the inverse of that seen in the conventional heat treatment in a furnace, resulting in the surface being cooler than the interior.[31] The MW treated slurry was then placed in a furnace for 4 hours at 800 °C. The heat-treated batch was then wet mixed using a pure ethanol medium and again MW treated for another 2 h at 300 °C. After the second MW treatment, the dried slurry was sintered at four different temperatures to obtain powdered samples. Part of the mixed batch was mixed with a Polyvinylidene fluoride (PVDF) binding agent and subsequently pressed into a pellet form. In the final stage, the pellets were sintered at four different temperatures from a 1000 to 1300 °C for 10 h after the second MW treatment, and the samples were ready for measurements.

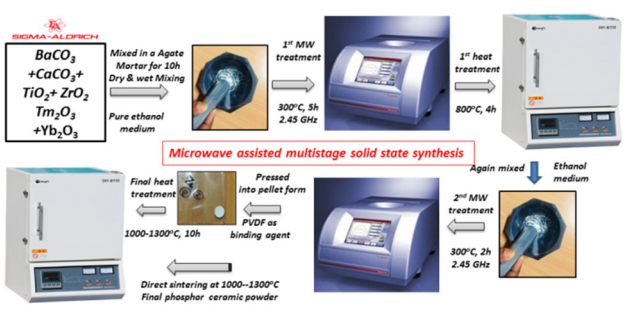

Fig. 1 Modified MW assisted multistage solid state synthesis flowchart of BCZT:Tm^{3+}/Yb^{3+} ceramic phosphor.

The synthesis technique of the green/red-emitting phosphor Er^{3+}/Yb^{3+}:BCZT can be found in the ESI.†

2.2 Characterization techniques

The crystal structure of the finely ground Tm^{3+}/Yb^{3+}:BCZT ceramic phosphor was recorded using a Bruker D8 advanced X-ray diffraction (XRD) measuring instrument with Cu-Kα target radiation (1.5405 Å) over a wide range of Bragg angles 2θ ($10° \leq 2\theta \leq 90°$) with a scanning rate of 3 deg per min. The UV-Vis NIR absorption spectrum was taken in diffuse reflectance mode on a Lambda 950, UV-VIS-NIR spectrophotometer (PerkinElmer). The UC luminescence characteristics of the Tm^{3+}/Yb^{3+}:BCZT samples at room temperature were investigated on a compact spectrophotometer with a dual-mode F980, Edinburgh Instruments for different 979 nm laser excitation power densities.

3 Results and discussion

3.1 Structural investigations

3.1.1 X-ray powder diffraction (XRD) study. The crystalline nature of the Tm^{3+}/Yb^{3+}:BCZT ceramic phosphors was analysed by recording the powder XRD patterns for different sintering temperatures. The diffraction patterns recorded for the samples sintered at 1000–1200 °C shows tetragonal crystal symmetry (*P4mm*) according to ICDD card no. 05-0626 of $BaTiO_3$.[23] However, the sample sintered at 1300 °C shows different crystal symmetry likely to be Rhombohedral (*R3m*), which is confirmed by the ICDD card no. 85-0368 of $BaTiO_3$. The related XRD pattern is shown in Fig. 2(a). It is noteworthy that, as the current perovskite ceramic host's A-site is formed with two elements *i.e.* Barium (Ba) 0.85% and Calcium (Ca) which is 0.15%, majority of the diffraction planes resembles with $BaTiO_3$ phase. To confirm more about the crystalline phase of the sample sintered at 1300 °C, we have rescanned the diffraction patterns. The region of the most intense diffraction planes *i.e.* 2θ value from 43–46° was scanned individually as shown at the Fig. 2(b).

The (200) diffraction peak was broad enough to be fitted with a Gaussian distribution, which led us to two peaks individually representing $(200)_{Tetragonal}$ and $(200)_{Rhombohedral}$. The results can be explained considering the co-existence of two

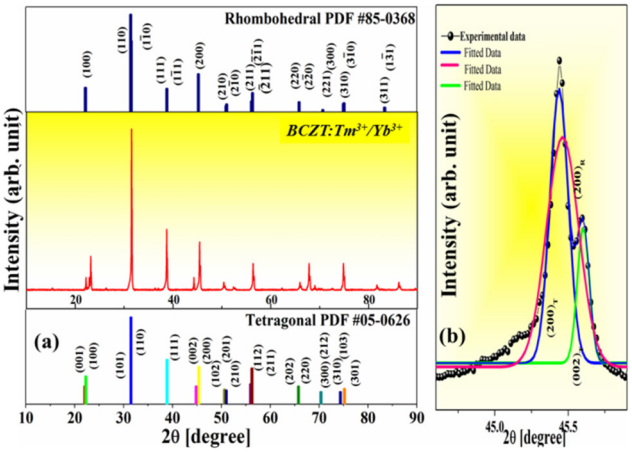

Fig. 2 (a) Powder X-ray diffraction pattern of Tm^{3+}/Yb^{3+} doped BCZT ceramic sample sintered at 1300 °C. (b) Gaussian fitted diffraction peak (200) scanned separately in the 2θ region 43–46°.

crystal symmetries together near MPB, with phase transforming from tetragonal to rhombohedral symmetry in the sample sintered at 1300 °C. The occurrence of the two different crystal symmetries is also supported by Rietveld analysis.

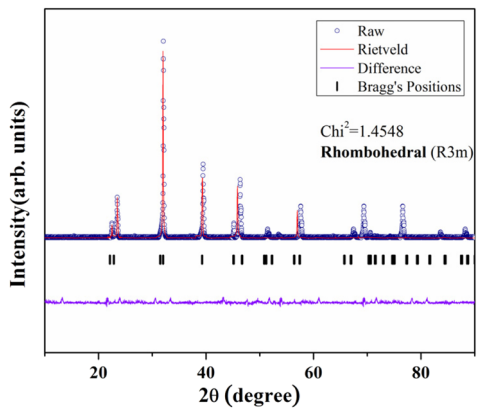

Fig. 3 Structural investigation and Rietveld refinement results for the Tm^{3+}/Yb^{3+} doped BCZT sample sintered at 1300 °C.

The Rietveld refinement was implemented using the FullProf Suite program (Free version) for improved structural information. The diffraction peak experiences into $(002)_T$ and $(200)_T$, indicating the presence of a tetragonal (T) phase (ICDD # 05-0626) with a space group of *P4mm* for the samples sintered at 1000–1200 °C. For sintering temperature 1300 °C, $(002)_T$ and $(200)_T$ these two peaks merges into a single one to indicate a rhombohedral symmetry. Moreover, in the rhombohedral symmetry the peak near $2\theta = 66°$ splits into two (220) and (202) respectively. The structural phase transition from tetragonal to rhombohedral is also confirmed by Rietveld refinements as shown in Fig. 3.

Rietveld refinement was performed using (Ba, Ca) (Zr, Ti)O_3 structure as a standard model, and the results of the refinements are shown in Table 1. The Rietveld refinement results for the samples sintered at 1000–1200 °C are shown in the ESI (see Fig. ESI 1).† The intermediate phases were also considered in the refinement process. The shifting of the diffraction peaks (002/200) towards lower 2θ values may be attributed to the larger ionic radius of Tm^{3+} (0.88 Å) compared to that of Ti^{4+} (0.68 Å), and Zr^{4+} (0.72 Å). The positions of the dopant ions (Tm^{3+}/Yb^{3+}) could not be determined directly through the refinement. The probable locations in the crystal structure can still be inferred. The most likely case is that the Tm^{3+} ions replaced the Ba^{2+} and another charge was compensated by the Ti^{4+} ion at the B-site. The reduced χ^2 value of the refined data was found to be 1.4548 for the sample sintered at 1300 °C and it confirms that a rhombohedral crystal symmetry has formed in the sample. The crystal phase transformation (tetragonal to rhombohedral) occurring in the sample increased the dopant ion transiting capabilities. A phase change from lower crystal symmetry to higher crystal symmetry is expected to help RE ion-dopants to give much better optical emission property. For our reference we have also recorded the XRD pattern for samples sintered at 1150 °C and 1250 °C to see any intermediate phase change or any change in diffraction peaks. The related plots are shown in Fig. (ESI 2).† The result shows no change in the diffraction peaks which confirms that the phase change occurs exactly at the 1300 °C sintering temperature.

The FESEM images of the Tm^{3+}/Yb^{3+}:BCZT samples sintered at four different temperatures are shown in ESI 3.† All

Table 1 Rietveld refinement fitting results and lattice parameter for the Tm^{3+}/Yb^{3+}:BCZT samples

	BCZT:Tm^{3+}/Yb^{3+}			
Lattice and fitting parameters	1300 °C	1200 °C	1100 °C	1000 °C
a (Å)	4.0059	4.0008	4.0064	4.0061
b (Å)	4.0008	4.0008	4.0064	4.0064
c (Å)	4.0123	4.0154	4.0064	4.0064
V (Å^3)	64.3	64.3	64.3	64.3
Structure	Rhombohedral	Tetragonal	Tetragonal	Tetragonal
Space group	*R3m*	*P4mm*	*P4mm*	*P4mm*
ICSD No.	85–0368	05–0626	05–0626	05–0626
Reduced χ^2	1.4548	1.7928	1.7926	1.7926
R_{wp} (%)	7.71	7.55	9.59	9.28
R_p (%)	6.33	4.23	5.41	6.23

the micrographs were taken with a 40.00 kX magnification with EHT at 5.00 kV and WD = 2.9 mm. All samples showed micrometer size particles. Since the samples were crushed for the measurements and dispersed on the sample holder, it is hard to comment about the porosity of the samples. As the sintering temperature was increased the smaller particles grew into larger particles. The sample sintered at 1300 °C has the largest particle size with well-defined grain boundaries. The average particle size increased from 0.4 to 1 μm.

3.2 Optical emission studies

3.2.1 Upconversion emission studies. The electronic transition spectra in the diffuse reflectance (DRS) mode were recorded to obtain exact excitations for the present sample and a plot of the UV-Vis spectrum is shown in the ESI 4.† As the 976 nm bands were strongly absorbed by the sample, we could possibly excite the sample with a 980 nm diode laser. The upconversion emission spectra of Tm^{3+}/Yb^{3+} co-doped BCZT ceramic phosphors under 980 nm NIR excitation were recorded for four samples, and blue emission was observed. The most intense emission band was observed at 479 nm, which was associated with the $^1G_4 \rightarrow {}^3H_6$ transition of the Tm^{3+} ions (visible spectral range). Other less intense, emission bands were observed at approximately 658 and 800 nm, and corresponding to the $^1G_4 \rightarrow {}^3F_4$ and $^3H_4 \rightarrow {}^3H_6$ transitions of Tm^{3+}, respectively. The recorded spectra are compared in Fig. 4. It is noticeable that the intensity of the emission band in the 450–500 nm region (transition $^1G_4 \rightarrow {}^3H_6$) is very high compared to the 800 nm emission corresponding to $^3H_4 \rightarrow {}^3H_6$ transition. In general, the most intense UC emission is observed at approximately 800 nm for the Tm^{3+} ion under 980 nm excitation. However, in the present case the observed results show an increment of the visible blue emission which is rare and advantageous. The intensities of all emission bands remained low for samples sintered at 1000 °C, 1100 °C and 1200 °C, according to a comparison of the UC emission spectra. However, the change observed in the UC emission intensity of the sample sintered at 1300 °C is very interesting. Almost 60 times enhancement in intensity was observed compared with the other samples. This change in emission intensity is very high when we compare the results with those of the Er^{3+}/Yb^{3+} codoped BCZT sample (see ESI 5†). As per our previous observations in RE doped perovskite oxide photoluminescence studies,[18,19,30] we can correlate these present enhancement with crystal phase dependent UC studies. The crystal phase transformation (from tetragonal to rhombohedral symmetry) occuring in the sample was confirmed by X-ray diffraction analysis. It is well known that emission intensity is greatly impacted by domain and grain boundaries due to light scattering; hence UC emission intensity can identify phase transition. However, it is worth mentioning, the accuracy factor depends on emission band shifting rather than direct emission intensity, as intensity has no direct relationship with decoding crystal structure information. Here the observed UC emission has two relational analogies by which we can claim the occurrence of phase transformation in the sample. One is the 479 nm blue emission band dominating the 800 nm NIR emission band (very rare); the other reason is almost 60 times the intensity hike. If only the crystallite size has increased with a higher sintering temperature, then there will be a gradual increase in the emission efficiency. The unexpected large emission intensity leap is due to the symmetry transformation that is rhombohedral to tetragonal phase when the sintering temperature increases from 1200 °C to 1300 °C. This symmetry transformation helped us to reach the overall goal of efficient blue UC emission which can be used as a base material for W-LEDs.

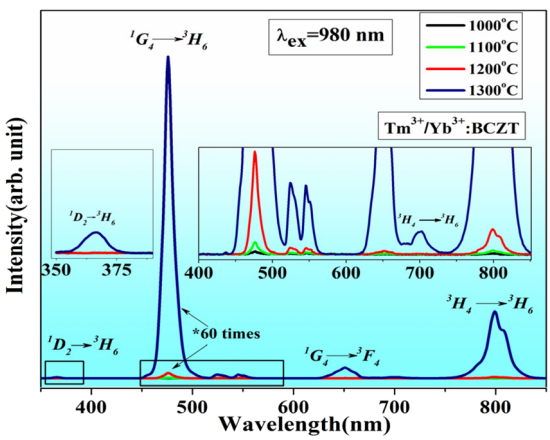

Fig. 4 Upconversion emission spectra with optical transitions of bands for Tm^{3+}/Yb^{3+}:BCZT ceramics at different sintering temperatures, measured at 980 nm diode laser excitations with P_{exc} = 35 W cm^{-2}.

3.2.2 Excitation power dependence study. To further study the excitation and emission processes, the involvement of the number of NIR photons for each emission band was studied. The UC emission intensity was recorded at different excitation powers (980 nm excitation). The graphs were plotted according to the procedure described in our previous reports.[32] The pump power dependence of the emission bands at 478, 658, 698, and 800 nm when the sample was excited by a 980 nm diode laser, is shown at Fig. 5. The graph clearly shows that the emission band at 479 nm varies smoothly with input power (shown in the inset). The double logarithmic plot of the UC emission intensity *versus* the excitation power density is also shown in the inset. The linear fitted slopes (n) were n_{479} = 1.39, n_{658} = 1.01 and n_{800} = 1.15. It was expected that the slope values for these emission bands should be around 2.0, but the experimental values were found to be less than 2. A possible reason for these proper values of 'n' can be understood by the fact that some phonon-assisted transitions also occur. The thermal quenching phenomena can also be considered and can be calculated for the exact integer number of photons, using the method demonstrated in our previous report.[33] The emission band at 478 nm has the highest slope value; hence, non-radiative transitions contribute the least. The slope values for the other bands were quite low, indicating the involvement of non-radiative channels.

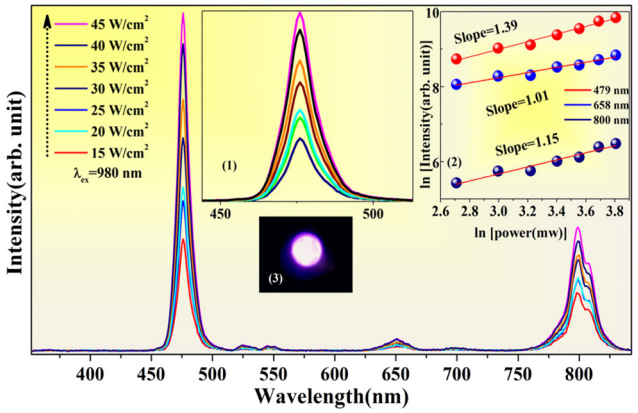

Fig. 5 Excitation power dependence UC emission spectra of the emission bands of Tm^{3+}/Yb^{3+}:BCZT ceramics. Inset (1) shows perfect Gaussian distribution of the 479 nm blue-emitting band from the sample. Inset (2) shows double logarithmic plots corresponding power density-dependent slope factors "*n*". Inset (3) shows intense blue emission from the sample (P_{exc} = 35 W cm^{-2}) directly visible through naked eyes, captured using digital mirror less camera.

3.2.3 Upconversion mechanism. Thulium-activated phosphors have complex energy-level structures. The reason for this kind of complicated energy level structure can be predicted as the strong deviation from R–S coupling in the 4f configuration; as a result the photon crosses through many paths and, ultimately, the relaxation of the excited levels of Tm^{3+} ions give rise to a wide variety of emission bands in the UV, visible, and IR regions. The UC mechanisms based on the Tm^{3+}/Yb^{3+} ion energy level diagram are shown in Fig. 6 and possible pathways are also discussed. The UC mechanism in Tm^{3+}/Yb^{3+} ions can be understood based on power-dependence studies. Detailed processes have already been discussed in our previous reports[30] and important steps are given here. The 980 nm excitation is very weakly absorbed by the Tm^{3+} ion, and hence singly doped Tm^{3+} ions give very weak UC emission. However, when the Yb^{3+} ions are co-doped, intense blue emission is observed from the Tm^{3+} ion, which can be explained based on cooperative energy transfer. In this case Yb^{3+} ions are excited to the $^2F_{5/2}$ level by absorbing 980 nm radiation. The two Yb^{3+} ions cooperatively join their energies and reach a virtual level of approximately 489 nm.

$$980\ \text{nm} = 10\,204\ \text{cm}^{-1}$$

$$10\,204\ \text{cm}^{-1} + 10\,204\ \text{cm}^{-1} = 20\,408\ \text{cm}^{-1} = 490\ \text{nm}$$

The energy from this virtual level was radiatively transferred to the $^1G_4$ level of the Tm^{3+} ion. The $^1G_4$ level relaxes further to lower levels and populates them. Also, at a small probability the process $^2F_{5/2}$ (Yb^{3+}) + $^3H_6$ (Tm^{3+}) → $^2F_{7/2}$ (Yb^{3+}) + $^3H_5$ (Tm^{3+}) also happens. The $^3H_5$ level quickly depopulates *via* multi-phonon relaxation to the lower lying $^3F_4$ level. The $^3F_4$ level absorbs 980 nm excitation and populates the $^3F_2$ level. The radiative emission wavelengths and associated transitions are shown in Fig. 6.

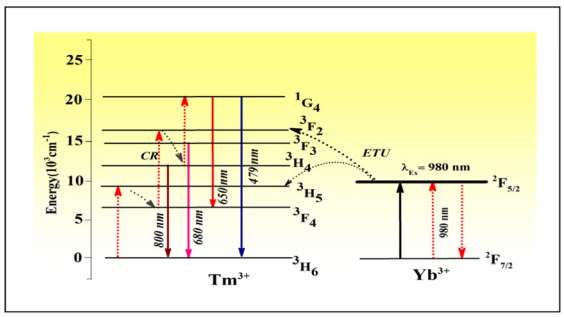

Fig. 6 Schematic illustrations of the energy level diagram using possible UC mechanism responsible for optical emissions.

3.2.4 Crystal phase transformed UC emission strategy. UC luminescence depends on the concentration and combination of dopants which define the number of luminescent centres as well as their spatial distance in the host material lattice. It has been reported that UC emission efficiency can be regulated by changing the crystal phase, size, and morphology of the host matrix and hope lies here. Rare-earth ions in a crystal experience electrostatic interactions and their magnitudes are dependent on the position of the ion in the structure of the crystal. Same ion in various crystal structures of a compound gives different emission intensity *e.g.* Er^{3+} ion in β-$NaYF_4$ gives very high UC emission compared to α-$NaYF_4$.[34,35] Here, the blue UC emission efficiency was tailored using this crystal phase modulation. The four samples were synthesised at four different sintering temperatures (1000–1300 °C) to investigate the crystal phase modulation activated by thermal heating near the MPB. The first three samples sintered at 1000–1200 °C respectively shows tetragonal symmetry (*P4mm*), whereas the sample sintered at 1300 °C exhibited rhombohedral symmetry (*R3m*). Interestingly the powder XRD patterns show that the sample at 1300 °C contains some additional peaks which match with the tetragonal symmetry. Therefore, we have tried to scan again for the sample sintered at 1300 °C and found the most intense diffraction peak (2 0 0) could be fitted in a Gaussian distribution into two peaks. Moreover the two fitted peaks has exact matching with 2θ values 44.5° of $(0\ 0\ 2)_R$ symmetry and 2θ = 44.9° of $(2\ 0\ 0)_R$ symmetry. The shape of crystal structure and atomic arrangement changed continuously during the heating process, especially the thermal activation energy is responsible for the change of crystal symmetry in this perovskite oxide ceramics near MPB region. The tetragonal phase of Tm^{3+}/Yb^{3+}:BCZT was activated by thermal activation energy and somewhat turned into higher rhombohedral crystal symmetry. An interesting observation was made during the powder XRD scan of the sample sintered at 1300 °C. Not only did the tetragonal symmetry gradually decrease along the increasing sintering temperature, at 1300 °C it coexisted with a new rhombohedral symmetry. It is well known that, near the morphotropic phase boundary, the existence of two phases is very unstable and usually lasts for a very short time. However,

for the present sample, the coexistence of the two phases emphasises the activation energy because the crystal lattice with higher symmetry shows exceptional replacement of Tm^{3+}/Yb^{3+} dopant ions into the lower symmetrical site. The atomic evolution during the phase transformation process from the tetragonal to metastable rhombohedral phase is supported by the idea that the activation energy of tetragonal symmetry is conserved and transferred to the next stable phase near the MPB. In the nano regime, a similar observation was made by Pin *et al.*[35] who demonstrated the transformation of Er^{3+}/Yb^{3+} doped UCNPs from the hexagonal phase to the stable cubic phase at the interface of the liquid similar to another unstable phase. In the present case, this was the sole reason for the excellent enhancement in luminescence observed for the sample at 1300 °C (almost ~60 times). Usually, the blue UC emission efficiency is one order of magnitude lower than the green/orange emission efficiency. However, the present ceramic phosphor sample utilised the replacement of optically active dopants, that is, Tm^{3+}/Yb^{3+} at the interface of two coexisting phases. Therefore, it is expected that the quantum efficiency of the blue-emission will be much higher than that reported previously. To the best of our knowledge, this type of structural phase modulation through atomic evolution has never been reported to correlate with any optical emissive properties, especially in UC emission studies.

3.2.5 UC quantum efficiency. The UC emission efficiency of the present sample was observed to further process its optical emissive properties for white-light applications. The UC luminescence quantum yield (Φ_{UC}) is defined by eqn (1):

$$\Phi_{UC} = \frac{q_{p.emission}}{q_{p.absorbed}} \quad (1)$$

Here, $q_{p.emission}$ is the upconverted emission photon flux (in photons per sec) and $q_{p.absorbed}$ is the photon flux absorbed by the sensitizer species (in photons per sec):

$$\Phi_{UC} = \frac{\int_{\lambda_1}^{\lambda 2} I_{uc}(\lambda)d\lambda}{q_{p.absorbed}} \quad (2)$$

Here, $I_{uc}(\lambda)$ is the emission intensity (in photons per sec per nm), and λ_1 and λ_2 represents the boundary wavelengths of the complete upconverted emission spectrum, or the 4f–4f transition of interest, respectively. $q_{p.absorbed}$ is calculated by integrating over the excitation wavelength range λ_3 to λ_4, and subtracting the intensity of the excitation source that has passed through the sample ($I_{exc\text{-}sample}$, in photons per s per nm) from the intensity of the excitation source that has passed through a blank sample (work as reference sample) ($I_{exc\text{-}blank}$). A dispersion of undoped BCZT sample of identical size distributed in the same solvent as the sample with the similar concentration was used as blank sample. Absence of optically active dopant makes it suitable for reference sample which doesn't absorb the excitation wavelength.

$$q_{p.absorbed} = \int_{\lambda_3}^{\lambda_4} [I_{exc\text{-}blank}(\lambda) - I_{exc\text{-}sample}(\lambda)]d\lambda \quad (3)$$

The eqn (2) can be expressed as,

$$\Phi_{UC} = \frac{\int_{\lambda_1}^{\lambda_2} I_{uc}(\lambda)d\lambda}{\int_{\lambda_3}^{\lambda_4} [I_{exc\text{-}blank}(\lambda) - I_{exc\text{-}sample}(\lambda)]d\lambda} \quad (4)$$

The spectrometer and the integrating sphere were calibrated such that the measured intensities are directly proportional to the photon flux, *i.e.* $(\lambda) \propto$ [mol of photons per s per nm]. As a result, integrating these values over the boundary wavelength range will directly count the flux of photons. Because the intensity of the upconverted light is lower than that of the stimulating laser source, the sample absorption and emission cannot be detected simultaneously, as the laser light saturates the spectrometer, preventing simultaneous measurement of UC. To overcome this, the absorption was measured using a neutral density (ND) filter with a specified transmittance (~99.85% attenuation). To measure the absorbed photon flux, this filter was added between the integrating sphere and the spectrometer. To remove the excitation light before measuring the upconverted emission, this filter was replaced with an OD4 short pass filter (875 nm). Over the wavelength range of the laser (950–990 nm), the attenuation factor F_{attn} was averaged. The short pass filter used to detect the intensity of the upconverted emission was also employed to account for the light's minimal absorption. The UC luminescence intensity was divided by the short pass filter's transmission curve $T(\lambda)$ in the wavelength range of the upconverted light. Due to the short pass filter's significant absorption of light with a wavelength shorter than 430 nm, this approach was unable to detect any UV emission. The accordingly corrected equation for Φ_{UC} is eqn (5):

$$\Phi_{UC} = \frac{\int_{\lambda_1}^{\lambda_2} \frac{I_{uc}(\lambda)}{T(\lambda)}d\lambda}{\int_{\lambda_3}^{\lambda_4} \frac{[I_{exc\text{-}blank}(\lambda) - I_{exc\text{-}sample}(\lambda)]}{F_{attn.}}d\lambda} = \frac{q_{p.emission}}{q_{p.absorbed}} \quad (5)$$

Fig. 7 shows the quantum yield for different samples measured based on eqn (1–5) using the above discussed setup. The quantum yield shown by the 479 nm blue UC emission was found to be the highest.

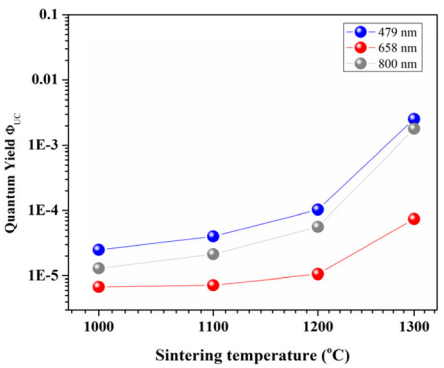

Fig. 7 Sample sintering temperature dependence of the absolute quantum yield Φ_{UC} of the major and minor emission bands of Tm^{3+}/Yb^{3+}:BCZT ceramics.

Moreover, the stability of the quantum yield can be determined by varying the pump power densities of the excitation pump. Quantum yields for a wide range of power dependencies were observed and plotted using the logarithmic relation shown in Fig. 8(a). The blue-emission band of Tm^{3+}/Yb^{3+}:BCZT exhibited the highest quantum yield over a wide range of pump power densities. These results also support the idea of crystal-phase-modified UC emission enhancement. To better understand the degradation and stability the quantum yield of the phosphors, we also investigated the QY in the Tm^{3+}/Yb^{3+}:BCZT thin films, as shown in Fig. 8(b). It is observed that the deposited phosphor thin film also shows the high yield values in the order of 1×10^{-3}. The results predicted that the current phosphor material could also be individually used as a commercial blue-emitting phosphor in device fabrication with higher emissivity. The deposition technique of the Tm^{3+}/Yb^{3+}:BCZT thin film on a Si- substrate is described in the ESI.†

3.2.6 White-light emission process. The generation of white-light using UC emission requires a combinational phosphor mixed in specific ratio, which is our technological interest. The high quantum efficiencies of the major emission band at 479 nm of Tm^{3+}/Yb^{3+}:BCZT ceramics show the great potential of its use in white-light generation if mixed with a green/red-emitting phosphor. The same stoichiometric composition was used to synthesise other Er^{3+}/Yb^{3+}:BCZT ceramics with optimised dopant concentrations reported in our earlier work[19,30] to produce green/red-emitting phosphors. The detailed synthesis process is discussed in the ESI.†

The UC emission studies of the Er^{3+}/Yb^{3+}:BCZT ceramic were performed using 980 nm CW laser irradiation. The ambient condition emission spectra of Er^{3+}/Yb^{3+}:BCZT ceramic samples sintered at 1300 °C are shown in figure (ESI 5†). Two intense green emission bands at 524 and 543 nm, assigned to the popular $^2H_{11/2} \rightarrow {}^4I_{15/2}$ and $^4S_{3/2} \rightarrow {}^4I_{15/2}$ transitions of trivalent erbium, respectively, were observed in the sample.

The UC emission spectra of the white-emitting biphasic sample under 980 nm excitations are presented in Fig. 9. In the visible range, three primary emission bands centred at 479, 550, and 673 nm were observed. Based on the RGB emissions, it was plausible to obtain multicolour emissions, including white-light by appropriately adjusting the dopant concentrations. All the samples had high emissions in the near-infrared range, centred at 800 nm. The compositions, x and y calculated colour coordinates, excitation power densities, and room-temperature UC efficiencies of the selected biphasic sample under 980 nm stimulation are listed in Table 2.

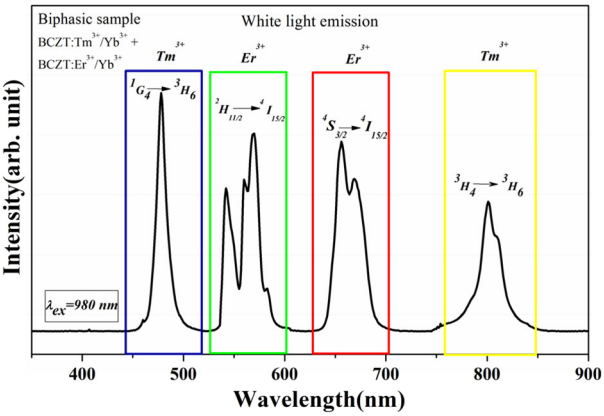

Fig. 9 Typical emission spectra of white emitting biphasic sample (Tm^{3+}/Yb^{3+}:BCZT + Er^{3+}/Yb^{3+}:BCZT) under 980 nm excitation.

At low excitation power densities (as low as 35 W cm^{-2}), biphasic materials generate white-light. Variations in the excitation power density had a little effect on the colour coordinates for a given sample composition (Table 2). The calculated chromaticity coordinates (x, y) are (0.331, 0.344), which are very close to the standard equal energy white-light co-ordinates (0.333, 0.333) according to the 1931 CIE diagram, (Fig. 11). Fig. 10 shows the images of the samples taken from a canon mirror-less camera with a longer exposure time of 5″, ISO 200 aperture f6.3 and exposure $+2^{1/2}$, when the samples irradiated with a 980 nm diode laser at the referred power densities. From the images, it was found that the biphasic sample (S_2) showed the maximum efficiency and intense white-light. The images were captured using an NIR filter and a neutral density (ND) filter which blocked the NIR emission from the samples. Images without the NIR filter appears to be reddish and can be seen in the ESI 6.† In addition, ESI 6† contains the (a) biphasic sample emission image with longer NIR exposure (laser induced heating) (b) emission image from the sample without NIR filter, (c) top view of the sample holder, (d) horizontal view of the sample holder in normal light (e) full 980 laser setup for recording the white emission.

The present biphasic material showed higher UC efficiencies of ~0.30% at power densities as low as 35 W cm^{-2} (Table 2) and ~0.40% at 40 W cm^{-2}. Conventionally, it has been found that blue-emitting phosphors are an order of magnitude lower than green- or orange-emitting phosphor. However, the present blue-emitting phosphor (Tm^{3+}/Yb^{3+}:BCZT) showed exceptional quantum efficiency at different power densities (Fig. 8), which was due to the crystal phase transformation occurring in the sample discussed above. Taking advantage of the crystal symmetry change occurring in

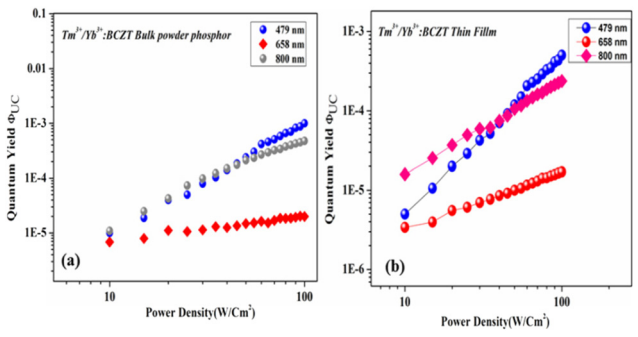

Fig. 8 Excitation power dependence of the absolute quantum yield Φ_{UC} of the major and minor emission bands of Tm^{3+}/Yb^{3+}:BCZT ceramics, (a) in bulk powder form, (b) in thin film deposited on p-type Si (100) wafer.

Table 2 Calculated colour coordinates, excitation power densities and room temperature UC efficiencies are presented below

Powder 1 (mass m_1) Tm^{3+}/Yb^{3+}:BCZT	Powder 2 (mass m_2) Er^{3+}/Yb^{3+}:BCZT	m_2/m_1 (sample acronyms)	P_{inc} (w cm^{-2})	x	y	η_{UC}
0.15%, 2.0%	0.2%, 2.0%	10(S_1)	35	0.329	0.343	0.30
		15(S_2)	45	0.331	0.344	0.35
		10(S_3)	40	0.348	0.341	0.40
		10(S_4)	45	0.313	0.343	0.35
		5(S_5)	45	0.313	0.333	0.33
		10(S_6)	30	0.311	0.333	0.27
		5(S_7)	30	0.321	0.333	0.25

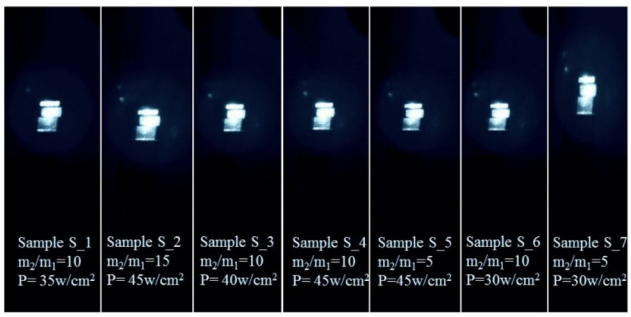

Fig. 10 Images of the biphasic samples with different combinational ratio with referred power densities.

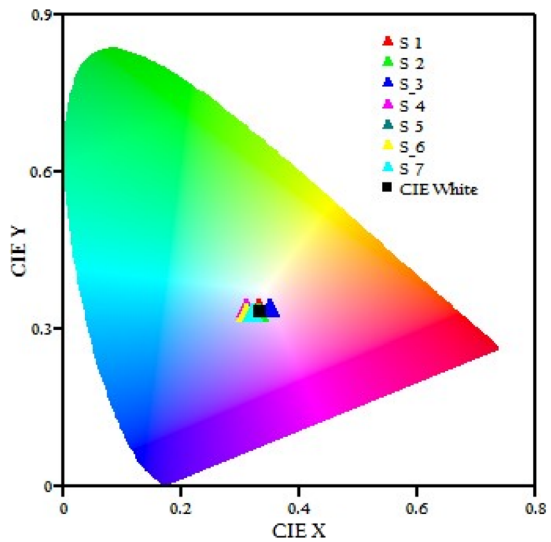

Fig. 11 The CIE 1931 chromaticity diagram of the biphasic samples with mixing ration referred at Table 1 with excitation of 980 nm lasers.

the sample, the blue-emitting phosphors can be efficiently employed in the white-light generation. Table 1 shows that to achieve white-light in biphasic materials, only 10 times more blue-emitting phosphors are required than green-emitting phosphors. Here, special emphasis is given to increase the efficiency of the blue-emitting phosphors *via* the crystal phase transformation occurring in the sample, which resulted in a significant increase in the overall white-light generation efficiency.

In three essential ways, we feel our samples are the best-reported white upconverting materials. First, as compared to materials for which UC efficiencies have been published; they exhibit greater blue UC emission efficiencies (Table 3). More importantly, the conventional blue-emission efficiency is significantly increased by using the crystal phase transformation from tetragonal to rhombohedral symmetry. This type of optical strategy has never been used to achieve white-light emissions. They also achieved high efficiencies when using lower excitation power densities than previously reported perovskite phosphor materials. It is worth noting that the power density for UC white-light generation and their efficiencies were not provided in many of the reports. For the reasons discussed above, the current biphasic ceramic phosphor (Tm^{3+}/Yb^{3+}:BCZT + Er^{3+}/Yb^{3+}:BCZT) is a promising candidates for a various applications, including display backlighting and WLED manufacturing.

3.2.7 Photometric characterizations. The present biphasic sample showed some interesting results for white-light emission. The optimal white chromaticity, according to the National Television Standard Committee (NTSC) standard, is around (0.33, 0.33). During the test, strong white-light emission was observed with the naked eye (Fig. 10). The quality of the white-light was assessed using the correlated colour temperature (CCT) for the application in commercial phosphor (w-LEDs). Using McCamy's empirical approach, the CCT value of the current phosphor was found within 5000–6000 K for the entire mixed ratio mentioned in the Table 1. The detailed formula and procedures were based on our previous work.[33] According to lighting industry convention, lamps with low CCT values (2700 K to 3000 K) provide light that appears "warm", while lamps having high CCT values (4000 K to 6500 K) provide light that appears "cool". Here the present biphasic phosphors show higher CCT and higher colour rendering index (CRI) near 90.56 which represents the potential for achieving cooler white-light appropriate for high quality lighting environments.

We further checked the colour purity of the biphasic samples from S_1 to S_7 to support "colour consistency" factor, a term used by the lighting industry utilizes a colour tolerance system in conjunction with CCT. Fig. 12 shows the colour purity calculation diagram of the different biphasic samples on the locus of the blackbody curve in the CIE diagram. The inorganic emissions of narrow-band lights are characterized by the dominant wavelength and colour purity,

Table 3 Compositions, excitation conditions, colour coordinates and UC efficiencies of white-light emitting materials reported in the literature

Host	Dopants	Excitations	CIE colour coordinate (x, y)	η_{UC}
Oxyfluoride glass ceramic doped with YF_3 nanocrystals[37]	Yb^{3+},Er^{3+},Tm^{3+}	976 nm pulsed laser (2 ps, 15 nJ, 2 W mm^{-2})	$x = 0.310$, $y = 0.359$	0.2
$BiPO_4$ submicron particles[38]	Yb^{3+},Er^{3+},Tm^{3+},Ho^{3+}	976 nm CW laser	$x = 0.318$, $y = 0.356$	
Tridoped YBO_3 phosphors[39]	Dy^{3+},Eu^{3+},Tb^{3+}	365 nm UV-LED laser	$x = 0.30$, $y = 0.33$	
$YNbO_4$ phosphors[40]	Yb^{3+},Er^{3+},Tm^{3+}	808 nm CW laser (2 W mm^{-2})	$x = 0.340$, $y = 0.359$	
Y_2O_3 nanocrystals[41]	Yb^{3+},Er^{3+},Tm^{3+}	976 nm pulsed laser (down to 100 mW cm^{-2})	$x = 0.310$, $y = 0.359$	
$Lu_3Ga_5O_{12}$ nanocrystals[42]	Yb^{3+},Er^{3+},Tm^{3+}	976 nm pulsed laser (down to 34 mW cm^{-2})	$x = 0.270$, $y = 0.338$	
Transparent oxyfluoride glass, ceramic embedded with YF_3 nanocrystals[43]	Yb^{3+},Ho^{3+},Tm^{3+}	976 nm pulsed laser (2 ps, 15 nJ, 2 W mm^{-2})	$x = 0.351$, $y = 0.306$	0.1
Fluorolead germanate glass[44]	Yb^{3+},Ho^{3+},Tm^{3+}	976 nm pulsed laser (2 ps, 15 nJ, 2 W mm^{-2})	$x = 0.344$, $y = 0.364$	
Tellurite glass[45]	Yb^{3+},Er^{3+},Pr^{3+}	976 nm pulsed laser (2 ps, 15 nJ, 2 W mm^{-2})	$x = 0.310$, $y = 0.335$	

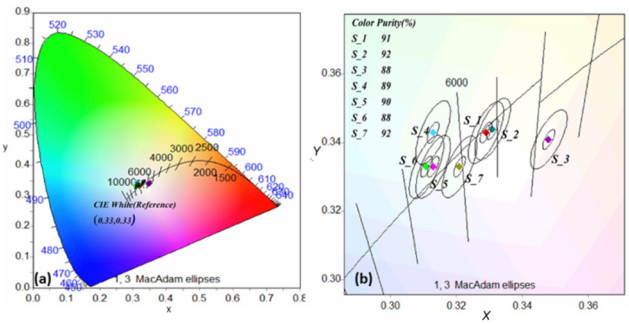

Fig. 12 (a) Colour purity calculation diagram in terms of the dominant wavelength. (b) Zoomed image of different biphasic phosphor samples on the locus of the blackbody in CIE diagram with reference colour purity.

whereas broadband lights are characterized by CCT. Colour purity was calculated using colour calculator software and the procedures were repeated as in our previous work.[33] The colour purity for all the samples retained a value within 88–92%, which is higher than reported in the literatures.[36] Therefore, biphasic sample combinations have the advantage of high colour purity and near-white colour coordinates with cooler white-light emissions, which can be employed readily for industrial lighting applications.

4 Conclusions

In pursuit of efficient upconverted white-light emission from RE ion-doped phosphors, two individual phosphors that are Tm^{3+}/Yb^{3+}:BCZT + Er^{3+}/Yb^{3+}:BCZT were mixed in a specific ratio (Table 2) and excited with a 980 nm CW diode laser. Tm^{3+}/Yb^{3+} co-doped BCZT ceramic phosphors were synthesised using a novel microwave assisted multistage solid state reaction route. The synthesis route and sintering temperatures were specially designed to observe the crystal phase change in the Tm^{3+}/Yb^{3+}:BCZT near the MPB. The quantum efficiency of 479 nm blue emissions was found to be exceptionally good on the verge of the crystal phase transformation occurring in the sample. Moreover, the quantum efficiencies of the blue phosphor were high in a wide range of excitation power densities (from moderate to high), implying that the stability of the blue emission was also high. A strategy to enhance the blue UC emission efficiency through crystal phase modulation was achieved, and biphasic phosphor samples were characterised by the addition of an Er^{3+}/Yb^{3+}:BCZT phosphor, which was optimized separately. White-light was generated in all samples mixed at different ratios (Table 2). It was found that only 10 times bluer phosphor than green phosphor is required to produce ideal chromatic white-light emission. Moreover, the current biphasic phosphor shows higher UC efficiencies of ~0.30% at power densities as low as 35 W cm^{-2} and ~0.40% at 40 W cm^{-2} (white-light emission through frequency UC), which is the best result ever reported to our knowledge. The main advantage of generating white-light through the referred process is that two different phosphors are optimized separately with threshold efficiency values; only their mixing ratio will determine the ultimate desirable results. The present samples emitted white-light at moderate low power with almost ideal white chromaticity with analogous to the NTSC standards. The blue emission (479 nm) intensity significantly increased in comparison to NIR (808 nm) wavelengths almost (x 60 times) upon sintering temperature change in Tm^{3+}/Yb^{3+}:BCZT and the anomalous behaviour is explained using the crystal phase transformation occurring in the sample. This improved UC strategy can be used to enhance white-light applications through structural modulation. Photometric characterisations show that the emitted white-light can be used as a cooler white-light source because of its observed higher CCT value (~5500 K) with a higher CRI value (90.56). The present biphasic phosphor has lab scale success in generating highly efficient (0.40%) upconverted white-light with a colour purity of ~92%; it is also expected that the present phosphor will be fruitful at the industrial scale.

Author contributions

The original idea, design, conceptualization of the work, experiments, Data analysis and interpretation and drafting of the article were done by PPS. Supervision, funding, resources, critical review, scientific suggestions and editing were done by HCS.

Conflicts of interest

The authors have no conflicts of interest to declare. All co-authors have seen and agree with the contents of the manuscript and there is no financial interest to report. We certify that the submission is original work and is not under review at any other publication.

Acknowledgements

The authors express their sincere thanks to the South African Research Chairs Initiative of the Department of Science and Technology and the National Research Foundation of South Africa (84415). The financial assistance from the University of the Free State, South Africa is highly recognized.

References

1 J. Wang and P. A. Tanner, *J. Am. Chem. Soc.*, 2010, **132**, 947–949.
2 C. Cao, Q. Liu, M. Shi, W. Feng and F. Li, *Inorg. Chem.*, 2019, **58**, 9351–9357.
3 K. Kim, S. K. Nam, J. Cho and J. H. Moon, *Nanoscale*, 2020, **12**, 12426–12431.
4 S. Asahi, H. Teranishi, K. Kusaki, T. Kaizu and T. Kita, *Nat. Commun.*, 2017, **8**, 14962.
5 J. Wang, N. He, Y. Zhu, Z. An, P. Chen, C. A. Grimes, Z. Nie and Q. Cai, *Chem. Commun.*, 2018, **54**, 591–594.
6 K. Li, D. Zhu and H. Lian, *J. Alloys Compd.*, 2020, **816**, 152554.
7 K. Li, D. Zhu and C. Yue, *J. Mater. Chem. C*, 2022, **10**, 6603–6610.
8 Y. Li, J. Zhang, Y. Luo, X. Zhang, Z. Hao and X. Wang, *J. Mater. Chem.*, 2011, **21**, 2895–2900.
9 B. Zhou, L. Tao, Y. H. Tsang and W. Jin, *J. Mater. Chem. C*, 2013, **1**, 4313–4318.
10 J. Li, Y. Long, Q. Zhao, S. Zheng, Z. Fang and B.-O. Guan, *Opt. Express*, 2021, **29**, 21763–21772.
11 J. Wang, R. Deng, M. A. MacDonald, B. Chen, J. Yuan, F. Wang, D. Chi, T. S. A. Hor, P. Zhang, G. Liu, Y. Han and X. Liu, *Nat. Mater.*, 2014, **13**, 157–162.
12 E. Downing, L. Hesselink, J. Ralston and R. Macfarlane, *Science*, 1996, **273**, 1185–1189.
13 H. M. Noh, J. H. Oh, J. H. Jeong, S. H. Park and B. C. Choi, *Curr. Appl. Phys.*, 2022, **39**, 190–195.
14 S. Sivakumar, F. C. J. M. van Veggel and M. Raudsepp, *J. Am. Chem. Soc.*, 2005, **127**, 12464–12465.
15 C.-W. Yeh, W.-T. Chen, R.-S. Liu, S.-F. Hu, H.-S. Sheu, J.-M. Chen and H. T. Hintzen, *J. Am. Chem. Soc.*, 2012, **134**, 14108–14117.
16 I. Etchart, M. Bérard, M. Laroche, A. Huignard, I. Hernández, W. P. Gillin, R. J. Curry and A. K. Cheetham, *Chem. Commun.*, 2011, **47**, 6263–6265.
17 F. Wang, Y. Han, C. S. Lim, Y. Lu, J. Wang, J. Xu, H. Chen, C. Zhang, M. Hong and X. Liu, *Nature*, 2010, **463**, 1061–1065.
18 P. P. Sukul, K. Kumar and H. C. Swart, *OSA Continuum*, 2018, **1**, 971.
19 P. P. Sukul, M. K. Mahata, U. K. Ghorai and K. Kumar, *Spectrochim. Acta, Part A*, 2019, **212**, 78–87.
20 A. Polman, *Physica B: Condens. Matter*, 2001, **300**, 78–90.
21 J. Rödel, W. Jo, K. T. P. Seifert, E.-M. Anton, T. Granzow and D. Damjanovic, *J. Am. Ceram. Soc.*, 2009, **92**, 1153–1177.
22 E. Cross, *Nature*, 2004, **432**, 24–25.
23 T. Karaki, K. Yan, T. Miyamoto and M. Adachi, *Jpn. J. Appl. Phys.*, 2007, **46**, L97–L98.
24 L. Dong, D. S. Stone and R. S. Lakes, *J. Appl. Phys.*, 2012, **111**, 84107.
25 A. De and R. Ranjan, *Mater. Horiz.*, 2020, **7**, 1101–1105.
26 I. Coondoo, N. Panwar, H. Amorín, V. E. Ramana, M. Algueró and A. Kholkin, *J. Am. Ceram. Soc.*, 2015, **98**, 3127–3135.
27 W. Liu and X. Ren, *Phys. Rev. Lett.*, 2009, **103**, 257602.
28 Z. Wang, W. Li, R. Chu, J. Hao, Z. Xu and G. Li, *J. Alloys Compd.*, 2016, **689**, 30–35.
29 Ramovatar, I. Coondoo, S. Satapathy and N. Panwar, *Ceram. Int.*, 2018, **44**, 1690–1698.
30 P. P. Sukul, Amitabh and K. Kumar, *OSA Continuum*, 2018, **1**, 1087–1096.
31 H. J. Kitchen, S. R. Vallance, J. L. Kennedy, N. Tapia-Ruiz, L. Carassiti, A. Harrison, A. G. Whittaker, T. D. Drysdale, S. W. Kingman and D. H. Gregory, *Chem. Rev.*, 2014, **114**, 1170–1206.
32 P. P. Sukul and K. Kumar, in Proceedings of SPIE - The International Society for Optical Engineering, 2017, vol. 10448.
33 P. P. Sukul, K. Kumar and H. Swart, *Dalton Trans.*, 2022, **51**, 2827–2839.
34 H. Dong, L. D. Sun and C. H. Yan, *Nanoscale*, 2013, **5**, 5703–5714.
35 M. W. Pin, E. J. Park, S. Choi, Y. Il Kim, C. H. Jeon, T. H. Ha and Y. H. Kim, *Sci. Rep.*, 2018, **8**, 2199.
36 Y. N. Ahn, K. Do Kim, G. Anoop, G. S. Kim and J. S. Yoo, *Sci. Rep.*, 2019, **9**, 16848.
37 D. Chen, Y. Wang, K. Zheng, T. Guo, Y. Yu and P. Huang, *Appl. Phys. Lett.*, 2007, **91**, 251903.
38 Z. Wang, J. Feng, M. Pang, S. Pan and H. Zhang, *Dalton Trans.*, 2013, **42**, 12101–12108.
39 K. Das, A. Marathe, X. Zhang, Z. Zhao and J. Chaudhuri, *RSC Adv.*, 2016, **6**, 95055–95061.
40 F. F. do Carmo, J. P. C. do Nascimento, M. X. Façanha and A. S. B. Sombra, *Mater. Lett.*, 2019, 65–68.
41 G. Y. Chen, Y. Liu, Y. G. Zhang, G. Somesfalean, Z. G. Zhang, Q. Sun and F. P. Wang, *Appl. Phys. Lett.*, 2007, **91**, 133103.
42 V. Mahalingam, F. Mangiarini, F. Vetrone, V. Venkatramu, M. Bettinelli, A. Speghini and J. A. Capobianco, *J. Phys. Chem. C*, 2008, **112**(46), 17745–17749.
43 D. Chen, Y. Wang, N. Yu, P. Huang and F. Weng, *J. Solid State Chem.*, 2008, **181**(10), 2763–2767.
44 A. S. Gouveia-Neto, L. A. Bueno, R. F. Do Nascimento, E. A. Da Silva, E. B. Da Costa and V. B. Do Nascimento, *Appl. Phys. Lett.*, 2007, **91**, 091114.
45 S. B. Rai, Y. Dwivedi and A. Ray, *J. Appl. Phys.*, 2008, **104**, 043509.